Case Studies in Chemical and Environmental Engineering 11 (2025) 101050

Contents lists available at ScienceDirect

Case Studies in Chemical and Environmental Engineering

journal homepage: www.sciencedirect.com/journal/case-studies-in-chemical-and-environmental-engineering

Case Report

Tunable copper based slag catalyst for energy vectors production

Stefano Savino [a], Giuseppe Guglielmo [b], Riccardo Muolo [a], Khaja Mohaideen Kamal [c], Fiorenza Fanelli [d], Giuseppe D'Amato [b], Paolo Bollella [a], Angelo Tricase [e], Michele Casiello [d], Rosella Attrotto [b], Blaž Likozar [c], Angelo Nacci [a,d], Lucia D'Accolti [a,d,*]

[a] Chemistry Department, Università degli Studi di Bari Aldo Moro, 70125 Bari, Italy
[b] Research and Development, Acciaierie d'Italia S.p.A., SS Appia km 648, 74123 Taranto, Italy
[c] National Institute of Chemistry, Department of Catalysis and Chemical Reaction Engineering, Hajdrihova 19, SI-1000 Ljubljana, Slovenia
[d] ICCOM-CNR, SS Bari, Via Orabona 4, 70126 Bari, Italy
[e] Pharmaceutical Science Department, University of Bari Aldo Moro, 70125, Bari, Italy

ARTICLE INFO

Keywords:
Steel slag
Photocatalysis
CO_2 reduction
Hydrogen production
Circular economy

ABSTRACT

Steel slag is known to contain various metal oxides and minerals that have the potential to function as green and sustainable catalysts for chemical reactions. Previous studies demonstrated that, albeit calcium aluminate is the major constituent, the presence of iron oxides enables the slag to function as photocatalyst for CO_2 reduction reaction (CO_2RR) to formic acid, and that doping with palladium improves these properties. In this new study, a novel and more versatile catalyst was prepared by functionalizing the slag with CuO nanostructures. The hybrid material (CuO-slag) was characterized by XRD, XPS, FESEM and SEM-EDX techniques, while electrochemical measurements certified its photocatalytic properties. Catalytic tests demonstrated that it is capable to convert CO_2 into formic acid in good yields (231 μmol $gcat^{-1}$ h^{-1}), but also to push reduction reaction up to methanol (81.5 μmol $gcat^{-1}$ h^{-1}) and ethanol (40 μmol $gcat^{-1}$ h^{-1}), the latter under photo-thermal conditions. Finally, to further extend the scope of the hybrid material, the hydrogen evolution reaction (HER) was also investigated.

1. Introduction

The rapid increase in atmospheric carbon dioxide levels due to human activities is a major contributor to global climate change. To mitigate climate change and minimize CO_2 emissions, it is crucial to develop sustainable and efficient technologies. The most known are certainly carbon dioxide capture and storage (CCS), and carbon dioxide capture and utilization (CCU) in chemical synthesis. The latter not only contributes to reducing global climate change but enables the conversion of carbon dioxide into new valuable resources, while at the same time exploits renewable energy and reduces wastes. In this field, some strategies are gaining importance, such as thermal catalysis, that usually requires harsh conditions to achieve high CO_2 conversions, through high-energy processes characterized by uncontrollable products selectivities [1]. Electrocatalysis strategies are another approach to CCU, albeit they suffer from the drawbacks of requiring complex apparatus and procedures as well as expensive membrane modules. In addition, these technologies, to be environmentally beneficial, must use renewable energy sources, to avoid secondary CO_2 emissions [2]. Other sustainable strategies are the biological fixation and the photo-thermal–photovoltaic synergistic catalytic CO_2 conversion. The latter is attracting attention in recent years, because can take advantage of solar energy which is free and abundant to achieve CO_2 photoreduction [3]. The photocatalyst, typically a semiconductor, captures light energy generating electron–hole pairs. These charge carriers participate in subsequent redox reactions at the catalyst surface, such as reducing CO_2 molecules adsorbed on the catalyst. At the same time, the holes oxidize water to produce oxygen (O_2) or other sacrificial agents in the reaction medium (Fig. 1).

Several types of photocatalysts are commonly used in CO2RR, such as MOF, doped TiO_2 materials (to improve photo-reactivity) and metal oxides [4]. In recent years, Cu-based catalysts have attracted attention due to their efficiency and selectivity in reducing CO_2 to CH_3OH and CH_4 [5]. Catalytic performance proved to be strictly related to the different kinds of Cu nanostructures employed, that are in turn dependent on their preparation procedures [6].

In addition, Cu nanoparticles (NPs) can function as cocatalysts in more complex hybrid materials. Typical examples are represented by

* Corresponding author. Chemistry Department, Università degli Studi di Bari Aldo Moro, 70125 Bari, Italy.
E-mail address: lucia.daccolti@uniba.it (L. D'Accolti).

https://doi.org/10.1016/j.cscee.2024.101050
Received 17 October 2024; Received in revised form 5 December 2024; Accepted 5 December 2024
Available online 6 December 2024

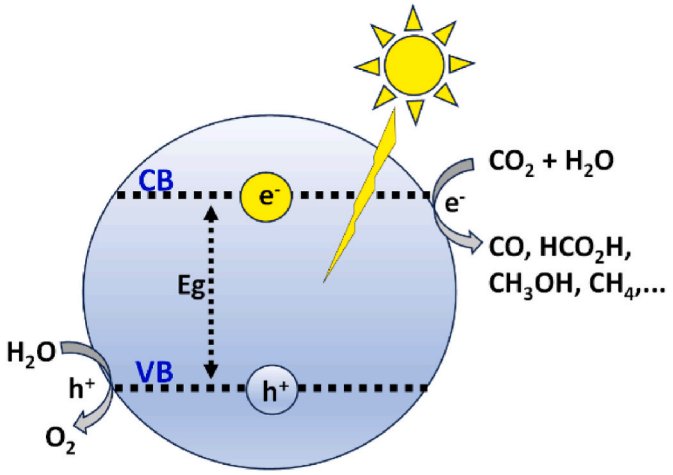

Fig. 1. Generic mechanism of a photoreaction.

zeolites-based composites with metal oxide nanoparticles, such as copper oxide (CuO), that are considered alternative photocatalytic materials in the CO_2 reduction process [7]. Notably, these composites can be obtained from waste such as volcanic ash following a circular economy approach.

In line with this strategy, very intriguing appeared to us the use of photocatalysts based on Ladle Furnace slag (LF slag), a safe, abundant and cheap residue of steel industry that seems to be ideal for industrial applications. This approach would allow the valorization of a large volume waste by converting it in a precious catalyst for CO_2RR, opening its application in a new field where the steel slag is almost unexplored.

During steel production processes, residues are inevitably generated which can be classified as waste or by-products based on their use after production. Among them, the "slags" play a fundamental role in the liquid steel production process as they allow the removal of unwanted components such as SiO_2, Al_2O_3, sulfur, and phosphorous. In particular, the LF slag used in this study arises from the Italian integral cycle steel plant (Acciaierie d'Italia), where it is produced during secondary treatments of steel, approximately in a quantity of 10–20 kg/ton of liquid steel. Indeed, according to EUROSLAG statistics, approximately 1.75 Mton of LF Slag were produced in Europe in 2021, constituting 14 % of Steel Furnace Slag (SFS) (i.e., all slags obtained from steel production excluding Blast Furnace Slag) [8].

Although Steel Furnace Slags are already recycled up to 80 %, their use is limited to that of inert material, especially in the construction field [9].

However, by virtue of their composition rich in metals, a better way to valorize this material is to transform it in an efficient and recyclable catalyst. Indeed, our previous studies have already shown that steel slags display catalytic properties in the CO_2 photoreduction process [10].

In addition, being composed of several oxides (e.g. SiO_2, Al_2O_3, Fe_3O_4, etc.) such materials can also act as a practical and effective support, particularly for non-critical metals, that can be compounded with the slag, leading to more efficient hybrid catalysts, avoiding tedious and costly synthetic processes.

The use of LF Slag as a catalyst is reflected in the production of biological and synthetic renewable fuels. These applications have already been demonstrated at laboratory level [10–12], reaching the double objective of improving the recycling procedures and increasing the sustainability rate of fuel production, thus contributing to the decarbonization of all those systems that are difficult to electrify.

Furthering developing this research line, in this study the LF Slag was thoroughly characterized by X-ray diffraction spectroscopy (XRD), X-ray photoelectron spectroscopy (XPS), scanning electron microscopy-energy dispersive X-ray spectroscopy (SEM-EDX) field emission-scanning electron microscopy (FESEM) to determine their composition and morphology, in addition in this new paper we determined the electrochemical properties to assess the photoreduction potentials, demonstrating that the slag could be considered a "*new semiconductor materials*." The properties of slag were enhanced using a low-cost material such as copper that allowed to further develop the resulting catalyst, applying the system in different reactions, tuning the obtainable solar fuels.

2. Materials and methods

Solvents and reagents were purchased from Sigma-Aldrich and used as received. Steel slag was provided by "Acciaierie d'Italia," the main Italian steel producer based on integrated steel production cycle (Taranto, Italy). This material constitutes the secondary slag (LF slag) arising from ladle treatments that are performed on the liquid steel iron to improve the quality characteristics of the final product. To assure the reproducibility of samples for catalytic tests, the slag coming from steel treatments plants was prepared in the ADI laboratories by grinding and homogenizing, in two steps, three different stocks to reach the particle size of 230 mesh (0.063 mm).

2.1. Material characterization

X-ray diffraction (XRD) spectra were acquired using SmartLab X-Ray diffractometer AdI & X'Pert MPD diffractometer (PANalytical). The powder X-ray diffraction (PXRD) spectra were registered at room temperature by depositing ground powders of each sample onto a Si wafer (zero background) which was rotated (0.5 Hz) during spectrum acquisition. The spectra were acquired with a X'PERT-PRO powder diffractometer, equipped with solid state detector (PIXcel) and a parabolic MPD mirror, using CuKα radiation (λ = 1.54059 A). The PXRD spectra were recorded in the 2 Theta range 4.00–90° applying a step size of 0.0263° and a counting time of 50.49 s. per step.) The samples were previously ground to reach a fine grain size suitable for analysis. They were subsequently housed in the sample holder and suitably flattened to increase the resolution of the peaks and avoid phenomena of background derivation and signal displacement. The diffractograms were acquired in a 2θ range between 10 and 90° and considering a speed of 0.5°/min.

X-ray photoelectron spectroscopy (XPS) analyses were performed by means of a PHI P5000 VersaProbe II scanning XPS microprobe spectrometer, equipped with a monochromatic Al Kα X-ray source (X-ray spot size = 100 μm, power = 23.3 W). Wide scans (0–1400 eV) and high-resolution spectra (C 1s, O 1s, Ca 2p, Al 2s, Al 2p, Fe 2p, Mg 2p, Mn 2p, Si 2p, Cu 2p, Cu $L_3M_{4,5}M_{4,5}$) were acquired in fixed analyzer transmission mode, with pass energy of 117.40 and 29.35 eV, respectively. Charge neutralization was constantly applied during spectra acquisition. The binding energy (BE) scale was referenced to the hydrocarbon component of the C 1s spectrum of adventitious carbon at 284.8 eV. MultiPak software (Version 9.5.0.8, October 30, 2013, Ulvac-PHI, Inc.) was used for data processing. Analyses were repeated on minimum three different spots per sample and the mean values are reported.

Field-emission scanning electron microscopy (FESEM) observations of the catalyst powders deposited onto a Si wafer were carried out with a Zeiss SUPRA™ 40 FESEM microscope (no sample metallization). Images were acquired at electron acceleration voltage (extra-high tension) of 3 kV, working distance of 2.0–2.5 mm, magnification up to 500 k ×, using an in-lens secondary electron detector.

Scanning electron microscopy-energy dispersive X-ray analyses (SEM–EDX, ADI laboratory) were performed with TESCAN AMBER X. Before SEM observations each sample was sputter-coated with 20 nm of C using a turbo-pumped sputter coater (Quorum Technologies, Lewes, UK, model Q150T ES plus). Images were acquired with the in-lens detector at a working distance in the range of 2.8–3.0 mm, electron acceleration voltage of 15 kV, beam current 1 nA and magnification in the range of 6–70 kX. Instead, EDX analysis were conducted with LE – BSE

(low energy – backscattered electrons) detector, using working distance of 6 mm and an electron acceleration voltage of 15 kV.

Electrochemical measurements were conducted in a gastight H-type cell with two compartments separated by a Nafion-117 anion exchange membrane, using a PalmSens4 electrochemical workstation equipped with PSTrace 5.6v software at room temperature. For photoelectrochemical measurements, the same system was utilized, equipped with a commercial solar simulator equipped with a Xenon arc lamp (300 W, Newport) and an AM 1,5G filter. The light source was positioned approximately 25 cm from the H-cell to maintain the electrolyte temperature between 25 and 30 °C. One compartment housed 70 mL of 0.5 M $KHCO_3$ electrolyte in DI water and a Pt wire counter electrode, while the other contained the same electrolyte, an Ag/AgCl reference electrode in saturated KCl solution, and the working electrode [13]. Typically, 10 mg of the catalyst and 5 mg of ketjenblack were dispersed in 0.48 mL isopropanol and 20 μL of a 5 wt% Nafion binder solution under sonication for 1 hour to create a homogeneous ink. Then, 100 μL of this ink was applied to a 1 × 1 cm^2 carbon fiber paper electrode. During measurements, the electrolyte was purged first with N_2 for 30 minutes to achieve its saturation (measurements performed in dark and light conditions), then with CO_2 for 30 minutes to achieve CO_2 saturation (pH = 7.2, measurements performed in dark and light conditions). Linear sweep voltammetry (LSV) was performed with a 10 mV s^{-1} scan rate from 0 V to −1.2 V vs. RHE in CO_2-saturated 0.5 M $KHCO_3$ electrolyte. All potentials were converted to the reversible hydrogen electrode (RHE) scale using the equation: E(vs. RHE) = E(vs. Ag/AgCl) + 0.059 × pH + 0.196 V. Additionally, the open circuit potential (OCP) was measured saturating the electrolyte with CO_2 in dark and light conditions to determine ΔE correlated with CO_2 photoelectroreduction.

Chemical composition of both the gas and liquid phase was assured by gas chromatography (GC). In details, a GC TRACERA instrument (Shimadzu) was used, equipped with a BID (Barrier Discharge Ionization) detector at Helium plasma and two kinds of columns: a DC-UIWAX column (30 m, 0.25 mm id, film thickness 0.25 μm) for polar compounds and a Restek widebore column (30 m, 0.25 mm id) for the gas phase. In addition, the gas phase was also analyzed with an SRI GC 8610C gas chromatograph, equipped with a thermal conductivity detector (TCD) and a flame ionization detector (FID), using a methanizer attachment and a high purity helium or nitrogen as a carrier gas.

2.2. Synthesis of CuO nanostructures

In order to functionalize the steel slag a literature procedure was followed to synthesize copper nanoparticles [6]. Considering the influence of the surface morphology in solar absorbance, different concentrations of NaOH were tried. Indeed, it was found [14] that the base strength employed during synthesis significantly influenced the morphological characteristics due to variations in reaction velocity and particle growth dynamics.

At first, three aqueous solutions of NaOH 0.5 M, 0.75 M, and 1.0 M were added in separate flasks, dropwise and under stirring, to an equal volume of 0.2 M solutions of $Cu(NO_3)_2{\cdot}3H_2O$.

Each single mixture turned into a light blue color and subsequently a blue color precipitate was formed, which indicated the generation of Cu $(OH)_2$ nanostructures. The resultant suspensions were filtered, washed several times with distilled water and dried at room temperature to get three different $Cu(OH)_2$ nanostructure precipitates.

These solids were heated in an oven at 80 °C for 1 h, generating the related CuO nanostructures. The as prepared CuO nanostructures were washed many times and dried at room temperature. Then, they were further calcined at 350 °C for 6 h, for a better crystallization. Subsequently, the CuO nanostructures were anchored over the LF steel slag as follows.

2.3. Functionalization of LF steel slag with CuO nanostructures

The CuO nanostructures were supported on the slag by impregnation leading to the final photocatalyst nanocomposites. In a typical procedure a slag/CuO 3:2 w/w ratio was applied. The starting materials were mixed under stirring for 24 h in a beaker containing methanol (50 mL per gram of starting materials). Next, the composites were filtered and washed to collect the solid part that was dried in oven at 80 °C for 24 h.

2.4. Reduction of functionalized catalysts

In order to explore different oxidation states of copper, a reduction process was tested putting the catalyst in a furnace tube with a flow of N_2 200 mL/min for 20 min, with the purpose of removing all the oxygen. After that time, the flow of N_2 was replaced with a H_2 flow of 200 mL/min. Reduction was investigated at three different temperatures (60–120–250 °C) for 2 h.

The list of the nanocomposite photocatalysts prepared is reported in Table 1.

2.5. Photocatalytic experiments

2.5.1. Photoreduction of CO_2

Typical procedure: in a 25 mL quartz flask, 0.03 g of photocatalyst were dispersed by sonication in 5 mL of water and the reactor was sealed. The suspension was thoroughly degassed by flushing CO_2 gas for 30 min to remove air and saturate the aqueous phase. Then, the suspension was irradiated for 5 h using a commercial solar simulator equipped with a Xenon arc lamp (300 W, Newport) and an AM 1.5G filter. Several experiments were conducted in an aqueous solution of NaOH 0.2 M. The liquid phase composition was analyzed with a gas chromatography equipped with a flame ionization detector (FID), which works well in particular for all organic compounds, and high purity helium was used as carrier gas. The instrument used for the analysis was Thermo Scientific (Focus GC, AS 3000).

2.5.2. Water splitting photoreaction (hydrogen production)

In a typical reaction, 20 mg of photocatalyst were suspended in 50 mL of aqueous solution containing 25 vol% of methanol and the mixture was sonicated for 30 min to obtain a well-dispersed particle suspension. Before the light irradiation, the quartz flask was sealed with a rubber septum and the reaction mixture was bubbled with a nitrogen flow for 40 min to remove oxygen. Finally, the sealed quartz flask was subjected to 5 h of irradiation with the solar simulator (see above). H_2 evolution was measured every hour. The generated gas composition was analyzed with a gas chromatography (GC, SRI-8610C) equipped with thermal conductivity detector (TCD) and high purity nitrogen was used as carrier gas.

Table 1
Summary of nanocomposite photocatalyst investigated.

Catalyst materials	Description
Slag	LF Slag from AdI
CuO-Slag-0.5	LF Slag impregnated with CuO nanoparticles synthetized with NaOH 0.5 M
CuO-Slag-0.75	LF Slag impregnated with CuO nanoparticles synthetized with NaOH 0.75 M
CuO-Slag-1	LF Slag impregnated with CuO nanoparticles synthetized with NaOH 1 M
CuO-R60-Slag	CuO-Slag reduced at 60 °C for 2hrs under H_2 flow
CuO-R120-Slag	CuO-Slag reduced at 120 °C for 2hr under H_2 flow
CuO-R250-Slag	CuO-Slag reduced at 250 °C for 2hr under H_2 flow

3. Results and discussion

3.1. LF slags characterization

First of all, the characterization of the LF Slag was led through X-ray diffraction analysis in order to obtain information about the crystalline structure and, consequently, about the elements and their oxidation state.

The mineralogical composition of the slag sample was determined by X-ray diffraction (XRD), and Fig. 3 shows the result. The main crystalline phases identified are mayenite ($12CaO{\cdot}7Al_2O_3$), quartz (SiO_2), Magnetite (Fe_3O_4) and Wüstite (FeO).

XPS analyses were conducted to investigate the surface chemical composition of the LF slag, confirming the presence of the elements identified from XRD spectra (Table 2). The BEs of the Ca $2p_{3/2}$ (347.4 ± 0.2 eV) and Al 2p (74.2 ± 0.2 eV) signals are in line with literature data for CaO, Al_2O_3 and calcium aluminates [15–19]. The Ca/Al atomic ratio is about 0.45, suggesting that the slag surface is more enriched in aluminium oxide compared to $12CaO{\cdot}7Al_2O_3$ stoichiometry. Fig. 4 reports the high-resolution Fe 2p XPS spectrum, that can be curve fitted with six components ascribed to Fe^{2+} and Fe^{3+}, in agreement with the presence of Fe_3O_4 and FeO [20–22]. In particular, the components due to Fe^{2+} are the Fe 2p core-level peaks at 709.5 ± 0.2 eV (Fe $2p_{3/2}$), 723.0 ± 0.2 eV (Fe $2p_{1/2}$), and the satellite signal at 714.2 ± 0.2 eV; while, the Fe^{3+} components are the Fe 2p core-level peaks at 711.5 ± 0.2 eV (Fe $2p_{3/2}$), 725.2 ± 0.2 eV (Fe $2p_{1/2}$), and the satellite peak at 717.5 ± 0.2 eV [20–22]. Overall, the curve-fitting results accounted for a Fe^{3+}/Fe^{2+} surface atomic ratio of about 1.9.

XRD and XPS analyses of LF slag show that the material is mainly composed of an insulator such as mayenite ($12CaO{\cdot}7Al_2O_3$) (Fig. 3), containing Fe_3O_4 around 1 %. Therefore, the photocatalytic properties are prominently attributed to the UV–Vis absorption ability of iron oxide species. This is supported by studies showing that the excited state of the charge transfer of the isolated oxometallic species $[Me^{(n-1)+}–O^-]^*$ in these insulator materials plays a similar role to that of the photo-generated electron-hole pairs in the semiconductor. In this case, the charge transfer excitation $[Fe^{+3}\text{-}O^{2-}] \rightarrow [Fe^{+2}\text{-}O^{-}]^*$ is expected to be the key process for the CO_2 photoreduction reaction [10,23].

3.2. Characterization of the functionalized slag

Functionalized LF slags were characterized by FESEM, XRD, and SEM-EDX techniques. FESEM analyses (Fig. 5) allowed appreciating that CuO morphology is highly affected by the synthesis conditions and, in particular, by the concentration of the NaOH solution used for the synthesis. A 0.5 M NaOH solution leads to the formation of leaf-like CuO nanostructures (Fig. 5a). Considering the solar energy conversion, these CuO nanostructures are advantageous thanks to the large surface area towards absorbing considerable quantity of heat energy from the solar radiation when compared to three-dimensional spherical nanoparticles [6].

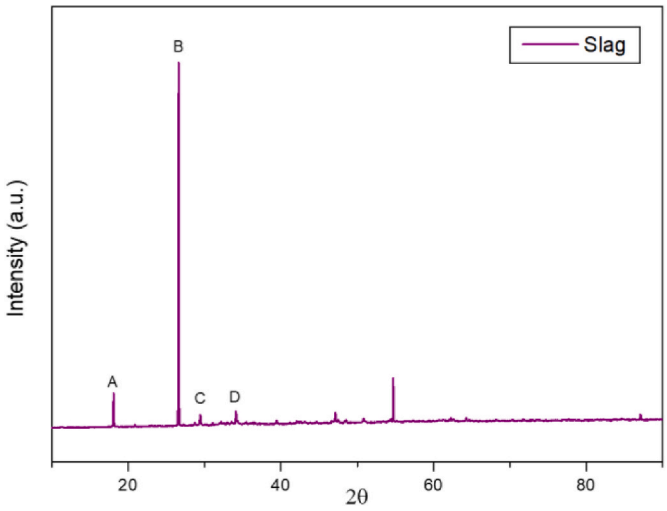

Fig. 3. XRD analysis of the LF slag, where A is Mayenite ($12CaO{\cdot}7Al_2O_3$), B Quartz (SiO_2), C Magnetite (Fe_3O_4) and D is Wüstite (FeO).

Table 2
XPS surface composition of LF Slag.

Sample Name	C (at %)	O (at %)	Ca (at %)	Al (at %)	Si (at %)	Mg (at%)	Fe (at %)	Mn (at%)
LF Slag	40	40	5.0	11.2	1.5	1.0	0.6	0.7

With the increase of NaOH concentration to 0.75 M, each nano-leaf is accompanied with nanoparticles deposited on the leaf-like structure (Fig. 5b). Having a relatively reduced size than that of the CuO nano-leaf, these nanoparticles increase the surface area for trapping significant proportion of heat energy from the incoming solar radiation.

The NaOH 1 M induces the transition to a morphology increasingly dominated by CuO nanoparticles, highlighting the correlation between the base strength and morphology (Fig. 5c).

The synthesis of the CuO nanostructures were replicated showing the same morphology, signifying a robust synthetic process.

Moreover, Fig. 6 shows the overlapped diffractograms of the analyzed samples of CuO-Slag-0.5, CuO-Slag-0.75 and CuO-Slag-1, where it clearly emerges the presence of the same reflections, indicating that the samples are composed of the same chemical complexes.

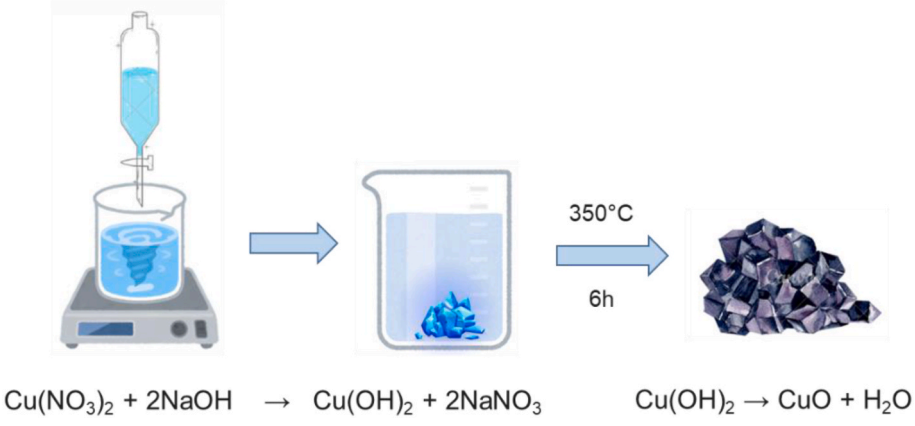

Fig. 2. Schematic synthesis of CuO nanostructures.

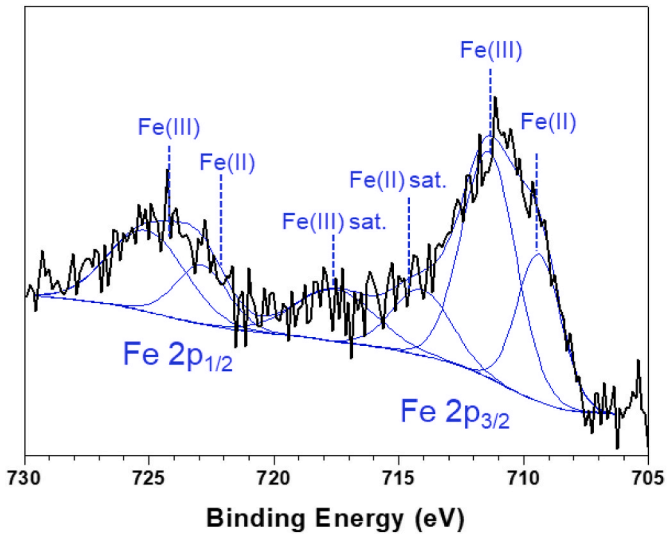

Fig. 4. High-resolution XPS Fe 2p spectrum of the LF slag.

By applying the Rietveld method, which includes a refinement of the parameters describing the crystal structures of each phase, the background and the shape of the peaks, it was possible to determine the mass percentage of the phases (Table 3). These data confirm the presence of copper throughout the surface meaning a correct inclusion of the nanostructure within the slag.

XRD analysis of LF slag samples functionalized with CuO shows the presence of copper in the form of oxide (Tenorite), mixed oxide (Papagoite) and of Copper(II)-Iron(III) oxide (Cuprospinel $CuFe_2O_4$). Such analysis also shows an increasing content of pure CuO, going from CuO-Slag-0.5 through CuO-Slag-1. This variance may be caused by the different morphology of CuO nanostructures (leaf-like or nanoparticles) adopted during the impregnation step. In addition, the considerable increase of copper oxide (61 % in CuO-slag 1), also coincides with the greater reactivity of the catalyst in the photoreduction of CO_2 as reported in Table 4.

As a mean to have a stronger confirmation of the XRD data, SEM-EDX analyses were performed in which it is possible to find a significant portion of copper well distributed across the sites and areas analyzed, confirming the effectiveness of the functionalization carried out (Figs. 7 and 1S).

Element	CuO-slag-0.5 (Wt%)	CuO-slag-0.75 (Wt%)	CuO-slag-1 (Wt%)
O	23.25	22.66	30.58
Mg	0.38	0.30	0.90
Al	13.63	18.28	11.83
Si	1.90	1.23	2.43
Ca	16.01	15.27	12.09
Mn	1.34	1.53	2.37
Fe	1.61	1.48	2.00
Cu	41.88	39.25	37.80
Total	100	100	100

From the catalytic experiments (*vide infra*) CuO-slag-1 clearly emerged as the best photocatalyst. Therefore, it was selected for the further investigations aimed at increasing the catalytic performance. In particular, it was subjected to reduction under hydrogen atmosphere at three temperatures, leading to the related reduced nanocomposites.

Fig. 8 shows the XRD spectra of the modified materials compared with those of the pristine slag and CuO nanostructures. The XRD pattern for CuO is consistent with the literature reports (JCPDS card number 1–1117) for the monoclinic structure of CuO. In the case of CuO-slag-1, XRD peaks refereed to CuO were found at 32.4°, 35.4°, and 38.6°, representing the (110), (002) and (111) planes, respectively.

The diffraction peaks at 26.6° and 29.4° originated from the mineralogical composition of the slag sample were also detected. For the composites produced at different reduction temperatures (60, 120, and 250 °C), all samples could be indexed by their chemical composition based on the available JCPDS files 1–1117 (CuO), and 1–1241 (metallic Cu). It was found that only a single-phase CuO was formed, when the reduction temperature was 60 °C. Metallic Cu was formed as an intense phase, although traces of CuO were also present in the samples reduced at 120 and 250 °C.

3.3. Electrochemical characterization of LF and functionalized slag

To estimate the catalytic properties of LF slag, open circuit potential (OCP) analysis were used. The ΔE correlated with CO_2 reduction and photoelectroreduction for LF slag modified electrode, were performed as reported in Fig. 9C. LF slag modified electrode shows a ΔE of 0.238 V for CO_2RR and a ΔE of 0.314 V for CO_2 photoelectroreduction (overall a ΔE of 0.552 V for the whole process). The overall ΔE of 0.552 V corresponds to an energy of 0.5 eV, which is close to the energy barrier for CO_2 reduction on magnetite, confirming the efficiency of LF slag towards CO_2RR. Although exact values for the energy barrier for CO_2 reduction on magnetite can vary, it is generally estimated to be in the range of 0.8–1.2 eV, depending on the reaction pathway and specific conditions [29,30].

In addition to compare the LF and functionalized slag (CuO-Slag-1, that showed the best performance (see the results in Table 4)), LSVs experiments were performed, to evaluate their catalytic activity in CO_2 reduction reaction (CO_2RR) and hydrogen evolution reaction (HER). Fig. 9A shows LSVs for LF slag modified electrode performed under N_2 saturated conditions (dark – solid black line and light – solid red line) and CO_2 saturated conditions (dark – solid blue line and light – dashed blue line) evidencing a great catalytic efficiency of LF slag towards CO_2RR over HER pathway.

The LF slag reported an onset potential (E_{ONSET}) for CO_2RR of −0.582 V vs. RHE. The catalytic current density at −1.2 V vs. RHE is −9.8 mA cm^{-2}. This can be correlated with the mineralogical composition because Magnetite (Fe_3O_4) and Wüstite (FeO) show a limited activity towards HER particularly at neutral pH (CO_2 saturated solution reported pH~7) compared with more conventional catalysts like platinum [31]. During CO_2RR, Magnetite (Fe_3O_4) ends to favour the production of formate ($HCOO^-$) and carbon monoxide (CO), with little tendencies to produce hydrocarbons and alcohols [32]. Magnetite

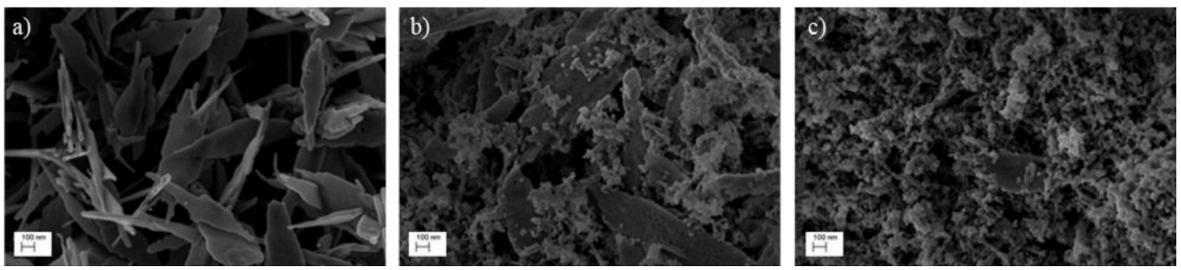

Fig. 5. FESEM images of CuO/slag nanocatalysts: a) CuO-slag-0.5, b) CuO-slag-0.75, c) CuO-slag-1.

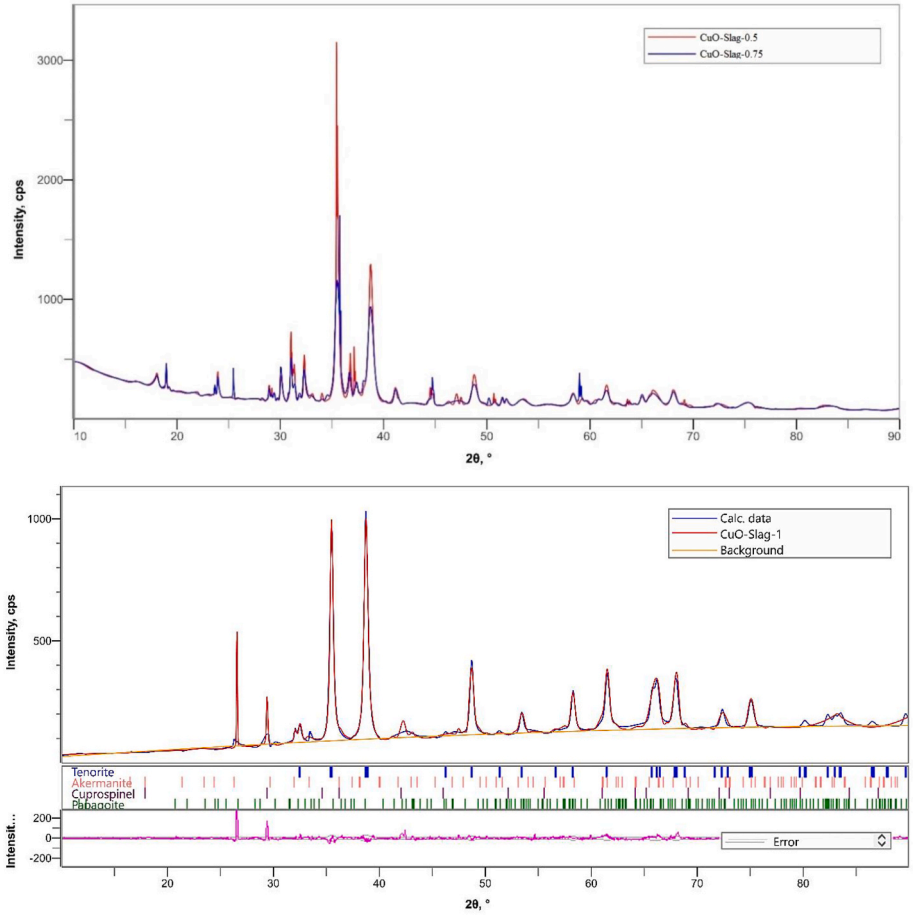

Fig. 6. Diffractograms of samples CuO-Slag-0.5, CuO-Slag-0.75 and CuO-Slag-1.

Table 3
Percentage of the weight fraction of the phases in CuO-Slag-0.5, CuO-Slag-0.75 and CuO-Slag-1.

Phases	Weight fraction of the phases (%)		
	CuO-Slag-0.5	CuO-Slag-0.75	CuO-slag-1
Tenorite, CuO	35	41	61
silicates-aluminium-calcium-magnesium, $Al_{6.5}Ca_5Mg_{0.75}Si_{0.75}O_{17}$	30	30	15
Papagoite, $AlCaCuSi_2O_9$	15	12	9
Cuprospinel, $Cu_{0.86}Fe_{2.14}O_4$	20	11	15

Table 4
CO_2 Photoreduction tests of functionalized LF slag/CuO catalytic materials.[a,b]

Entry	Catalyst	Formic acid (μmol·g_{cat}^{-1}·h^{-1})	Methanol (μmol·g_{cat}^{-1}·h^{-1})	Reference
1	Slag	54 ± 3	–	This work
2	CuO	–	10.7 ± 0.5	This work
3	CuO-Slag-0.5	330 ± 18	70 ± 4	This work
4	CuO-Slag-0.75	110 ± 5	66 ± 3	This work
5	**CuO-Slag-1**	**231** ± 12	**82** ± 4	**This work**
6	CuO-Slag-1 2nd Cycle	303 ± 16	61 ± 3	This work
7	Eu-MOF	304	–	[24]
8	Pd/slag	540	–	[10]
9	CdS/ZnS	320	–	[25]
10	g-C_3N_4	–	114	[26]
11	ZnO/CuO	238	traces	[27]
12	Cu_2O	–	1.2	[28]

[a] Reaction conditions: 5 mL CO_2 saturated water solution, 0.03 g of catalyst, room temperature, irradiation time 5 hours (see materials and methods).
[b] The blank reaction was occurred in same reaction condition. Each experiment was replicated three times.

(Fe_3O_4) is relatively stable under CO_2RR conditions, which is advantageous for prolonged operation [33]. The CO_2RR on magnetite involves multiple electron transfer steps and adsorption of intermediates on the catalyst surface. The presence of Fe^{2+} and Fe^{3+} sites in magnetite provides active sites for the adsorption and reduction of CO_2 [34].

Upon light activation, the LF slag showed an increasing of catalytic current of 1 mA cm^{-2} with a more positive E_{ONSET} at −0.468 V. The above-mentioned results suggest that the presence of Magnetite (Fe_3O_4) and Wüstite (FeO) deposited onto carbon-based electrodes can effectively harvest photons in visible light to achieve long-lived excited states and rapidly transfer the excited electrons to the Fe^{3+}/Fe^{2+} mixed core under light irradiation, thus supporting CO_2RR.

To increase the efficiency of Magnetite (Fe_3O_4) and Wüstite (FeO), LF slag was further functionalized with CuO that is well-known catalyst for CO_2RR [35,36]. Fig. 9B shows LSVs for functionalized slag modified electrode performed under N_2 saturated conditions (dark – solid black line and light – solid red line) and CO_2 saturated conditions (dark – solid blue line and light – dashed blue line) displaying both CO_2RR and HER activities. However, the functionalized slag reported an E_{ONSET} for CO_2RR of −0.502 V vs. RHE that is more positive than the HER E_{ONSET}. Additionally, the catalytic current density for CO_2RR is −16 mA cm^{-2} at −0.75 V vs. RHE, which is higher than the HER catalytic current density confirming that CO_2RR is still predominant.

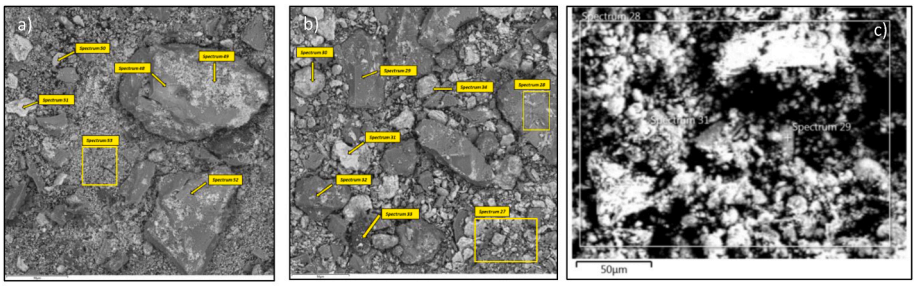

Element	CuO-slag-0.5 (Wt%)	CuO-slag-0.75 (Wt%)	CuO-slag-1 (Wt%)
O	23.25	22.66	30.58
Mg	0.38	0.30	0.90
Al	13.63	18.28	11.83
Si	1.90	1.23	2.43
Ca	16.01	15.27	12.09
Mn	1.34	1.53	2.37
Fe	1.61	1.48	2.00
Cu	41.88	39.25	37.80
Total	100	100	100

Fig. 7. SEM-EDS images and composition of a) CuO-Slag-0.5, b) CuO-Slag-0.75, c) CuO-Slag-1.

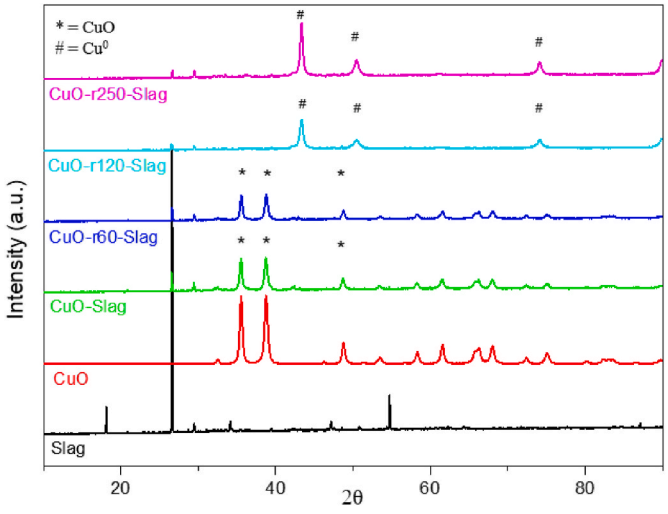

Fig. 8. XRD images of pristine slag (black), nanostructured CuO coming from synthesis with NaOH 1 M (red), CuO-slag-1 (green), CuO-slag-1 reduced at 60 °C (blue), CuO-slag-1 reduced at 120 °C (light blue), CuO-slag-1 reduced at 250 °C (purple). * = CuO related signals, # = characteristic peaks of Cu^0 (metallic copper).

Upon light activation, the functionalized slag showed a negligible increase in terms of catalytic current while the E_{ONSET} remains unchanged. This confirms that copper exhibits notable activity toward both HER and CO_2RR [37].

However, copper is well-known for its unique capability in catalysing the CO_2RR. This is due to its ability to facilitate the formation of a wide range of hydrocarbons and alcohols, which are valuable products of CO_2 reduction [38,39]. While several metals can catalyse HER effectively, copper stands out for its balanced activity and selectivity in converting CO_2 into useful chemicals, making it a prominent material for CO_2RR. Indeed, the functionalized slag showed four-times the catalytic current density of LF slag at −0.75 V vs. RHE highlighting the role of CuO towards CO_2RR.

The data obtained highlight how the potential values of the CuO-Slag catalyst are consistent with the photoreduction of CO_2 in formic acid and methanol in accordance to equations (1)–(4) below.

$$\text{CuO-Slag} \rightarrow \text{CuO-Slag}(e^-_{CB}) + \text{CuO-Slag}\ (h^+_{CB}) \quad (1)$$

$$2\ \text{CuO-Slag}\ (h^+_{CB}) + H_2O \rightarrow 2H^+ + 1/2O_2 \quad (2)$$

$$CO_2 + 2H^+ + 2\ e^- \rightarrow HCOOH \quad (3)$$

$$CO_2 + 6H^+ + 6e^- \rightarrow CH_3OH + H_2O \quad (4)$$

3.4. Screening of catalysts for photo-reduction of CO_2

Photocatalytic experiments were started with blank reaction, which certified that slag based catalysts under investigation are truly catalyst for this process (see note b in Table 4). The slag materials functionalized with CuO were tested in the photo-reduction of CO_2 and the catalytic activity was compared with that of pristine materials and of the literature (Table 4). Formic acid and methanol were the main products detected, and blank reactions (Table 4, entries 1–2) demonstrated that pristine LF slag favored exclusively formic acid while CuO led to the methanol production. Quantification of the photoreduction products was conducted by GC-BID using calibration curves (Figs. 2S and 3S).

In addition, due to the expected synergic effect, we anticipated that hybrid catalytic material should afford to increased yields of reduction products with ratios dependent on the morphology of copper oxide nanostructures. Results corroborated these assumptions showing that the leaf-like CuO nanostructures present in the CuO-Slag-0.5 catalyst (Fig. 5a) afforded the highest quantity of formic acid (Table 4, entry 3), while the nanosphere-structured CuO-Slag-1 (Fig. 5c) allowed achieving the highest production of methanol (Table 4, entry 5). These results show how the different morphology of the composites represents a crucial factor in the selectivity of the products, where surface roughness and size can govern the optical properties of the catalyst [6].

From these results clearly emerged the CuO-Slag-1 composite as the most efficient system for producing methanol and simultaneously satisfactory yields of formic acid. Therefore, it was selected for further experimentation.

Recycling experiment was carried out by filtration and drying of catalyst material that was prompted reused. The simultaneous production of both formic acid and methanol was still observed, even if with a slight increase of the former to the detriment of methanol (Table 4, entry

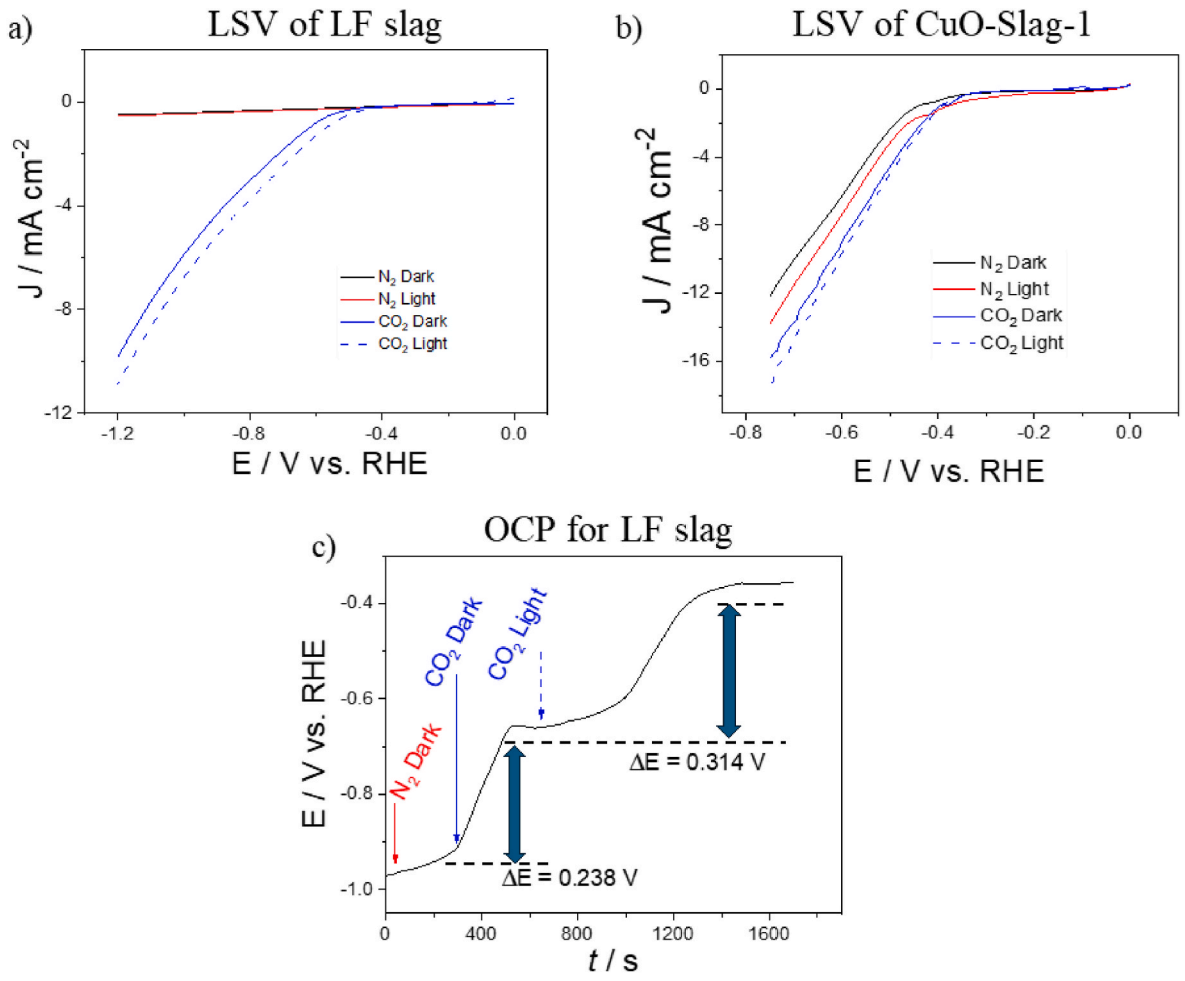

Fig. 9. a) LSV curves of LF slag modified electrode in N_2-saturated (dark – solid black line and light – solid red line) and CO_2-saturated (dark – solid blue line and light – dashed blue line) 0.5 M $KHCO_3$ solution scanned at scan rate 10 mV s^{-1}. **b)** LSV curves of CuO functionalized slag modified electrode in N_2-saturated (dark – solid black line and light – solid red line) and CO_2-saturated (dark – solid blue line and light – dashed blue line) 0.5 M $KHCO_3$ solution scanned at scan rate 10 mV s^{-1}. **c)** OCP for LF slag modified electrode measured in 0.5 M $KHCO_3$ solution in N_2-saturated (dark – solid red arrow) and CO_2-saturated (dark – solid blue arrow and light – dashed blue arrow).

6).

Comparison with the literature highlights the promising properties of this slag/CuO catalyst. Being a cheap and relatively nontoxic material, it can be considered competitive with analogous expensive systems based on rare metals (i.e. Eu-MOF and Pd, Table 4, entries 7–8) or on toxic metals (CdS and ZnS, Table 4, entry 9). In addition, due to its simple preparation procedure, it can compete for methanol production with well-known efficient catalysts such as Carbon nitride (g-C_3N_4) graphene composites (Table 4, entry 10).

The surface chemical composition of the CuO-Slag-1 catalyst was investigated by XPS before and after use in CO_2 photoreduction catalysis. Table 5 shows a decrease of the Cu surface atomic concentration from 15.5 at% to 9.5 at% after use, indicating a certain Cu loss during reaction. However, the high-resolution XPS Cu $2p_{3/2}$ spectra in Fig. 10 confirm the presence of CuO on the surface of the CuO-Slag catalyst before and after reaction. In particular, they present a main peak centered at 933.4 ± 0.2 eV in agreement with literature data for CuO, and the characteristic shake-up satellites (938–946 eV) for Cu^{2+} species [40–42].

Therefore, the XPS analysis of mapping data highlights how CaO, alumina, Fe and Cu remain equally distributed on catalyst surface after reactions, ensuring the reproducibility of the recycling process.

Table 5
XPS surface composition of CuO-slag catalyst (synthesized with 1 M NaOH solution) before and after use in photocatalytic CO_2 conversion.

Sample Name	C (at %)	O (at %)	Ca (at%)	Al (at %)	Si (at %)	Mg (at%)	Cu (at %)
CuO-Slag	18.5 ± 0.5	55.0 ± 1.0	2.5 ± 0.3	7.0 ± 0.6	1.0 ± 0.3	0.5 ± 0.2	15.5 ± 0.5
CuO-Slag after use	20.0 ± 1.5	56.0 ± 1.2	1.7 ± 0.2	11.5 ± 1.0	1.0 ± 0.2	0.3 ± 0.3	9.5 ± 1.0

3.5. *Photo-thermoreduction of CO_2*

To expand the reaction scope of LF slag/CuO catalyst, other factors such as temperature and pH were evaluated. To increase the amount of dissolved CO_2 in water, the pH was raised to 8, carrying out photoreduction in a NaOH 0.2 M aqueous solution. Surprisingly, the increase of pH caused the formation of ethanol (Table 6, entry 3) which proved to be competitive with some literature analogous (e.g. $Bi_{19}S_{27}Cl_3$, Table 6, entry 4), while only few example were reported for the production of ethanol using Copper catalysts, but only in electro-catalysis [43].

In order to increment the ethanol production, experiments on temperature dependence were conducted showing a direct correlation between the two factors (Table 6, entries 6–7). This allowed us to get better results in comparison to very recent results (e.g. In_2O_3/Cu–O_3, Table 6, entry 5).

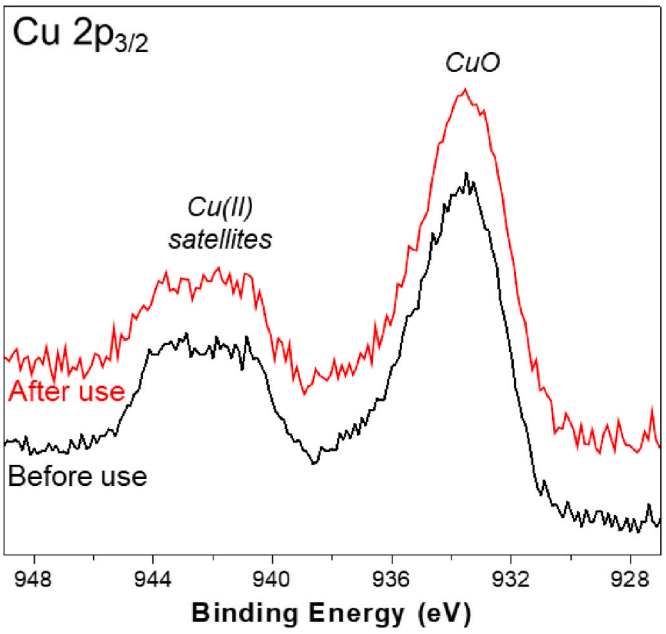

Fig. 10. High-resolution XPS Cu $2p_{3/2}$ spectra of the CuO-slag catalyst before and after use in CO_2 photoreduction.

Table 6
Influence of temperature and pH.[a]

Entry	Catalyst	Solvent	T (°C)	Ethanol (μmol·g_{cat}^{-1}·h^{-1})	Reference
1	–	NaOH/H_2O 0.2 M	25	-[b]	This work
2	CuO-Slag-1	H_2O	25	-[c]	This work
3	CuO-Slag-1	NaOH/H_2O 0.2 M	25	6.7 ± 0.8	This work
4	$Bi_{19}S_{27}Cl_3$	H_2O	25	5.2	[44]
5	In_2O_3/Cu–O_3	H_2O	25	20.7	[45]
7	CuO-Slag-1	NaOH/H_2O 0.2 M	60	12.0 ± 1.1	This work
8	CuO-Slag-1	NaOH/H_2O 0.2 M	80	40 ± 3	This work

[a] Reaction conditions: 50 mL CO_2 saturated water solution, 20 mg of catalyst, room temperature, irradiation time 5 hours (see materials and methods).
[b] Same result at 80 °C.
[c] Trace amounts detected at 80 °C.

A plausible route for ethanol formation is that its formation to formate is already formed via a 2-electron reduction step (Eq. (5)). Then, formate in turn can be further reduced to ethanol via multi-electron uptake step (Eq. (6)). In parallel, water serves as electron and proton donor (Eqs. (7) and (8)).

$$2CO_2 + 4H^+ + 4e^- \rightarrow 2HCOO^- + 2H^+ \quad (5)$$

$$2H_2O \rightarrow O_2 + 4H^+ + 4e^- \quad (6)$$

$$2HCOO^- + 10H^+ + 8e^- \rightarrow C_2H_5OH + 3H_2O \quad (7)$$

$$4H_2O \rightarrow 2O_2 + 8H^+ + 8e^- \quad (8)$$

The overall reaction is $2HCOO^- + H_2O + 2H^+ \rightarrow C_2H_5OH + 2O_2$ [46]

In light of this consideration, the conversion of CO_2 in ethanol in our case maybe could be favored in basic conditions because under almost neutral or strongly alkaline conditions CO_2 can be more easily converted into HCO_3^- and CO_3^{2-}, and both species are able to act as hole scavengers according to the following reaction:

$$HCO_3^- + h^+ \rightarrow HCO_3^{\bullet} \quad (9)$$

$$CO_3^{2-} + h^+ \rightarrow CO_3^{\bullet -} \quad (10)$$

Preventing recombination and improving overall photoreduction efficiency [47].

A similar effect was obtained by increasing the temperature, similar to semiconductor photoreaction, where the charge carrier recombination decelerates as temperature increases [48].

3.6. Photocatalytic H_2 production

To further extend the general applicability of LF slag/Cu hybrid materials, the hydrogen evolution reaction (HER) was also investigated in absence of CO_2. At this end, CuO-Slag-1 was subjected to the heating under hydrogen atmosphere to perform the reduction $Cu^{(II)} \rightarrow Cu^{(0)}$, being this latter the suitable species for carrying HER process, as co-catalyst [49].

XRD analyses allowed to monitor the oxidation number that Copper assumed varying the reduction temperature (Fig. 7). Three different reduced materials, labeled as CuO-r60-slag, CuO-r120-slag, and CuO-r250-slag, obtained after reduction in H_2 atmosphere for 2 h at 60 °C, 120 °C, and 250 °C, respectively, were selected for HER tests (Fig. 11).

Both time profiles (Fig. 11a) and yields trend (Fig. 11b) show that CuO-r250-slag displayed the best reducing activity in the hydrogen evolution reaction (HER), which is an expected result based on the highest Cu^0 content of this material due to the highest temperature conditions (250 °C) adopted during reduction. Notably, blank experiment carried out only with the CuO nanoparticles in the absence of slag, showed the absolute lack of hydrogen evolution, even after 5 h, thus confirming the importance of the slag in this process. This data was in accordance with the poor stability of Cu metallic nanoparticles. They have relatively little application in photocatalysis, while in our case the slag seems to play a role in the metal stabilization [49]. In the photocatalytic decomposition of water into hydrogen, however, metallic Cu acts as an electron collector, able to give H_2 production [49,50] also with methanol, as the sacrificial agent (Table 7, entry 1).

Comparison of hydrogen evolution activity (Table 7) with some reported slag-Cu based photocatalysts, highlights how the CuO-r250-Slag proposed in the current study can successfully compete with analogous materials in the literature, reported in Table 7.

4. Conclusion

LF slag proved to be an efficient photocatalyst in CO_2 reduction (CO_2RR) and hydrogen evolution (HER) processes (Fig. 9) by virtue of its mineralogical composition and an appropriate doping process with copper oxide nanoparticles. Indeed, the presence of Magnetite (Fe_3O_4) and Wüstite (FeO) (Fig. 3) enabled the slag to behave as an efficient photon harvesting material in the visible light range, triggering the CO_2 reduction to formic acid, as also evidenced by the electrochemical experiments. Moreover, treatment of the slag with nanostructured CuO, through an appropriate dosage, resulted in a four-time increase in the current density and simultaneously pushed forward the CO_2 reduction capacity from formic acid to methanol. In this regard, crucial proved to be the CuO nanostructures morphology (e.g. leaf-like or nanospheres) achieved through different synthetic conditions (Fig. 5).

In comparison to previous work where we obtained methanol after thermocatalysis reaction [10], LF slag/CuO hybrid composite proved to be a versatile catalytic material, capable of giving, in a one pot reaction under basic and photothermal conditions (80 °C and pH = 8), ethanol as reduced product. In addition, this new catalyst, after reduction at 250 °C under H_2 atmosphere, became an efficient photocatalyst for hydrogen evolution reaction (HER).

Results obtained in this study represent a virtuous example of waste valorization, where a large-volume residue of steel industry is

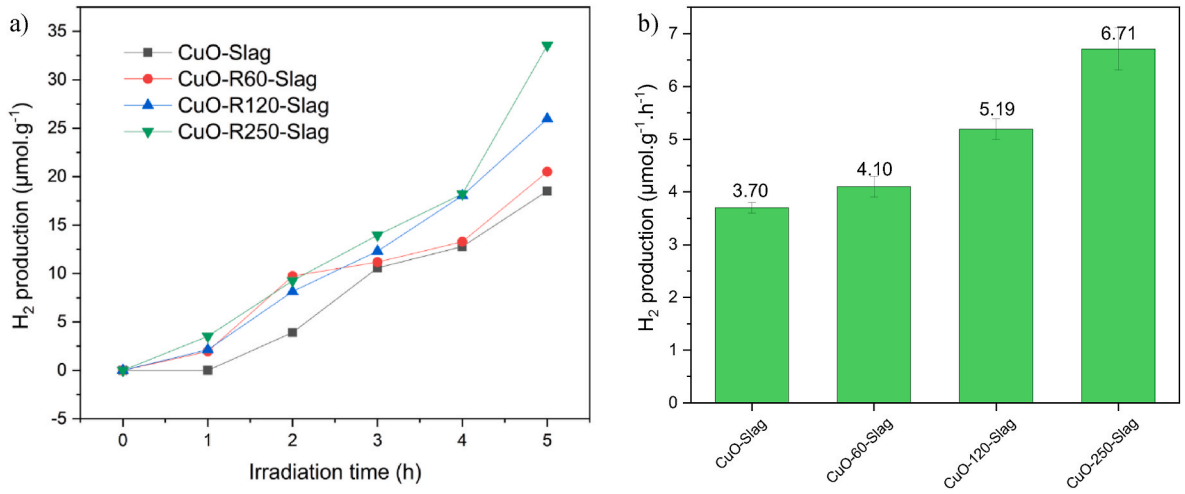

Fig. 11. a) Time profiles and b) yields of H_2 evolution over the studied photocatalysts.

Table 7
Comparison of hydrogen production activities of various reported slag photocatalysts with current study.

#	Photocatalyst	Sacrificial agent	Light	H_2 evolution rate (μmol·g^{-1}·h^{-1})	Ref.
1	Cu-Slag	Methanol	300W Xenon lamp	0.867	[51]
2	Cu-Slag	Acetic acid	Mercury vapor lamp	4.350	[52]
3	CuO-r250-Slag	Methanol	300W Xenon lamp	6.71	Present work

transformed in a precious catalyst useful for renewable fuels production (HCO_2H, CH_3OH, CH_3CH_2OH, and H_2) with an efficiency that is comparable with that of many literature analogous materials, often instead constituted by expensive and difficult to find compounds.

In conclusion, the present work aims to develop a possible process that can address the following problems at the industrial level: energy dependence on fossil fuels, thanks to the production of several solar fuels; reduction of carbon dioxide emissions, indeed the studied process blocks carbon dioxide in a cycle, preventing freeing it in the atmosphere; the cost, supply and disposal of commercial catalysts: the most commonly used catalysts are often made with expensive and difficult to produce materials, instead LF slag (used in this work) is a cheap material and available in large quantities. It is in fact a residue of the steel industry composed of the same oxides present in soil and rocks, so it is also a safe and environmentally friendly material that contributes to mitigation of waste production.

Finally, preliminary studies for hydrogen production have been presented, and the results obtained are encouraging for a future investigation of this aspect of the reactivity of the hybrid material LF slag/Cu.

CRediT authorship contribution statement

Stefano Savino: Writing – review & editing, Writing – original draft, Investigation, Data curation, Conceptualization. **Giuseppe Guglielmo:** Writing – review & editing, Software, Data curation. **Riccardo Muolo:** Writing – review & editing, Investigation. **Khaja Mohaideen Kamal:** Writing – review & editing, Investigation. **Fiorenza Fanelli:** Writing – review & editing, Software. **Giuseppe D'Amato:** Writing – review & editing, Investigation, Data curation. **Paolo Bollella:** Writing – review & editing, Formal analysis, Data curation. **Angelo Tricase:** Writing – review & editing, Formal analysis, Data curation. **Michele Casiello:** Writing – review & editing, Investigation. **Rosella Attrotto:** Writing – review & editing, Methodology. **Blaž Likozar:** Writing – review & editing, Methodology. **Angelo Nacci:** Writing – review & editing, Writing – original draft, Methodology, Data curation. **Lucia D'Accolti:** Writing – review & editing, Writing – original draft, Data curation, Conceptualization.

Declaration of competing interest

"There are no conflicts to declare".

All data are incorporated into this article and its online ESI material: the data underlying this article are available in the article in its online ESI† material.

Acknowledgements

This work was supported by the MASE (Ministero dell'Ambiente e della Sicurezza Energetica, ITALY) Project WASP grant number H93C22000360004.

Appendix A. Supplementary data

Supplementary data to this article can be found online at https://doi.org/10.1016/j.cscee.2024.101050.

Data availability

All data were reported in manuscript and ESI.

References

[1] W.D. Shafer, et al., Increased CO2 hydrogenation to liquid products using promoted iron catalysts, J. Catal. 369 (2019) 239–248.
[2] A. Bayon, et al., Techno-economic assessment of solid-gas thermochemical energy storage systems for solar thermal power applications, Energy 149 (2018) 473–484.
[3] W. Wang, et al., Photocatalytic CO2 reduction over copper-based materials: a review, J. CO2 Util. 61 (2022) 102056.
[4] H.Q. Wang, et al., Developments and challenges on enhancement of photocatalytic CO2 reduction through photocatalysis, Carbon Resources Conversion 7 (3) (2024).
[5] M.A. Avila-López, E. Luevano-Hipólito, L.M. Torres-Martínez, CO2 adsorption and its visible-light-driven reduction using CuO synthesized by an eco-friendly sonochemical method, J. Photochem. Photobiol. Chem. (2019) 382.
[6] P. Agalya, et al., Facile and low-cost synthesis of diverse copper oxide nanostructures for solar to thermal energy conversion, Optik 244 (2021) 167499.
[7] J.R.C. Sousa, et al., Development of photocatalysts based on zeolite A with copper oxide (CuO) for application in the artificial photosynthesis process, J. Environ. Chem. Eng. 11 (5) (2023).
[8] A. Gómez-Goiri, I. Gutierrez-Aguero, D. Garcia-Estevez, Leveraging blockchain usage to enhance slag exchange, Applied Sciences-Basel 14 (14) (2024).
[9] L. Jacob, Ladle furnace slag: synthesis, properties, and applications, ChemBioEng Rev. 11 (1) (2024) 60–78.

[10] C. Fusco, et al., Steel slag as low-cost catalyst for artificial photosynthesis to convert CO2 and water into hydrogen and methanol, Sci. Rep. 12 (1) (2022) 11378.
[11] M.S. Barbarey, et al., Utilization of ladle furnace slag for fabrication of geopolymer: its application as catalyst for biodiesel production, Construct. Build. Mater. 411 (2024) 134226.
[12] M. Casiello, et al., Steel slag as new catalyst for the synthesis of fames from soybean oil, Catalysts 11 (5) (2021) 619.
[13] Q.J. Wu, et al., Photocoupled electroreduction of CO2 over photosensitizer-decorated covalent organic frameworks, J. Am. Chem. Soc. 145 (36) (2023) 19856–19865.
[14] J.C. de Almeida, et al., Unveiling the influence of alkaline modifiers in CuO synthesis on its photocatalytic activity for CO2 reduction, Materials Advances 5 (16) (2024) 6479–6488.
[15] M. Ni, B.D. Ratner, Differentiation of calcium carbonate polymorphs by surface analysis techniques - an XPS and TOF-SIMS study, Surf. Interface Anal. 40 (10) (2008) 1356–1361.
[16] G. Chiarello, et al., An XPS study of SO2 ON A CaO surface derived from Ca(OH)2, J. Electron. Spectrosc. Relat. Phenom. 50 (2) (1990) 229–237.
[17] B.R. Strohmeier, Gamma-alumina (γ-Al2O3) by XPS, Surf. Sci. Spectra 3 (2) (1994) 135–140.
[18] R.K. Pan, S. Feng, H.Z. Tao, XPS and NMR analysis on 12CaO·7Al2O3, IOP Conf. Ser. Mater. Sci. Eng. 167 (1) (2017) 5.
[19] L. Kalina, et al., XPS characterization of polymer–monocalcium aluminate interface, Cement Concr. Res. 66 (2014) 110–114.
[20] D. Cappus, et al., Polar surfaces of oxides - reactivity and reconstruction, Surf. Sci. 337 (3) (1995) 268–277.
[21] N.S. McIntyre, D.G. Zetaruk, X-ray photoelectron spectroscopic studies of iron oxides, Anal. Chem. 49 (11) (1977) 1521–1529.
[22] L. Ouyang, et al., A surface-enhanced Raman scattering method for detection of trace glutathione on the basis of immobilized silver nanoparticles and crystal violet probe, Anal. Chim. Acta 816 (2014) 41–49.
[23] F. Shabib, et al., Hierarchical mesoporous plasmonic Pd-Fe3O4/NiFe-LDH composites: characterization, and kinetic study of a photodegradation catalyst for aqueous metoclopramide, Environ. Technol. Innovat. 27 (2022).
[24] T.-C. Zhuo, et al., H-Bond-Mediated selectivity control of formate versus CO during CO2 photoreduction with two cooperative Cu/X sites, J. Am. Chem. Soc. 143 (16) (2021) 6114–6122.
[25] H. Pan, M.D. Heagy, Photons to formate: a review on photocatalytic reduction of CO2 to formic acid, Nanomaterials 10 (12) (2020) 2422.
[26] R.C. Sahoo, et al., Bandgap engineered g-C3N4 and its graphene composites for stable photoreduction of CO2 to methanol, Carbon 192 (2022) 101–108.
[27] E. Luévano-Hipólito, L.M. Torres-Martínez, A. Fernández-Trujillo, Ternary ZnO/CuO/Zeolite composite obtained from volcanic ash for photocatalytic CO2 reduction and H2O decomposition, J. Phys. Chem. Solid. 151 (2021).
[28] Y.A. Wu, et al., Facet-dependent active sites of a single Cu2O particle photocatalyst for CO2 reduction to methanol, Nat. Energy 4 (11) (2019) 957–968.
[29] R. Bonetto, F. Crisanti, A. Sartorel, Carbon dioxide reduction mediated by iron catalysts: mechanism and intermediates that guide selectivity, ACS Omega 5 (34) (2020) 21309–21319.
[30] B. Singh, et al., Single-Atom (Iron-Based) catalysts: synthesis and applications, Chem. Rev. 121 (21) (2021) 13620–13697.
[31] X. Lu, et al., Multistep kinetic study of magnetite reduction by hydrogen based on thermogravimetric analysis, Int. J. Hydrogen Energy 73 (2024) 695–707.
[32] F. Mirabella, et al., CO2 adsorption on magnetite Fe3O4 (111), J. Phys. Chem. C 122 (48) (2018) 27433–27441.
[33] D.M.F. Clara Pereira, Andreia F. Peixoto, Marta Nunes, Bruno Jarrais, Iwona Kuzniarska-Biernacka, Cristina Freire, Hybrid carbon-metal oxide catalysts for electrocatalysis, biomass valorization and, wastewater treatment: cutting-edge solutions for a sustainable world, in: J.W. Sons (Ed.), Catalysis for a Sustainable Environment: Reactions, Processes and Applied Technologies, 2024.
[34] J. Pavelec, et al., A multi-technique study of CO2 adsorption on Fe3O4 magnetite, J. Chem. Phys. 146 (1) (2017).
[35] Y.C. Lan, et al., Electrochemical reduction of carbon dioxide on Cu/CuO core/shell catalysts, Chemelectrochem 1 (9) (2014) 1577–1582.
[36] W.W. Guo, et al., Highly efficient CO2 electroreduction to methanol through atomically dispersed Sn coupled with defective CuO catalysts, Angew. Chem. Int. Ed. 60 (40) (2021) 21979–21987.
[37] X.Y. Feng, et al., Metal-organic frameworks significantly enhance photocatalytic hydrogen evolution and CO2 reduction with earth-abundant copper photosensitizers, J. Am. Chem. Soc. 142 (2) (2020) 690–695.
[38] G.H. Simon, C.S. Kley, B. Roldan Cuenya, Potential-dependent morphology of copper catalysts during CO2 electroreduction revealed by in situ atomic force microscopy, Angew. Chem. Int. Ed. 60 (5) (2021) 2561–2568.
[39] Y.H. Wang, J.L. Liu, G.F. Zheng, Designing copper-based catalysts for efficient carbon dioxide electroreduction, Adv. Mater. 33 (46) (2021).
[40] C.C. Chusuei, M.A. Brookshier, D.W. Goodman, Correlation of relative X-ray photoelectron spectroscopy shake-up intensity with CuO particle size, Langmuir 15 (8) (1999) 2806–2808.
[41] M.C. Biesinger, et al., Resolving surface chemical states in XPS analysis of first row transition metals, oxides and hydroxides: Sc, Ti, V, Cu and Zn, Appl. Surf. Sci. 257 (3) (2010) 887–898.
[42] D. Barreca, A. Gasparotto, E. Tondello, CVD Cu2O and CuO nanosystems characterized by XPS, Surf. Sci. Spectra 14 (1) (2007) 41–51.
[43] R.M. Cai, et al., Engineering Cu(I)/Cu(0) interfaces for efficient ethanol production from CO2 electroreduction, Chem 10 (1) (2024).
[44] K. Das, et al., Intrinsic charge polarization in Bi19S27Cl3 nanorods promotes selective C?C coupling reaction during photoreduction of CO2 to ethanol, Adv. Mater. 35 (5) (2023) 2205994.
[45] S. Gong, et al., Electronic modulation of a single-atom-based tandem catalyst boosts CO2 photoreduction to ethanol, Energy Environ. Sci. 16 (12) (2023) 5956–5969.
[46] S. Ali, et al., Activity, selectivity, and stability of earth-abundant CuO/Cu O/Cu0-based photocatalysts toward CO2 reduction, Chem. Eng. J. 429 (2022), https://doi.org/10.1016/j.cej.2021.131579.
[47] G. Mele, et al., Photoreduction of carbon dioxide to formic acid in aqueous suspension: a comparison between phthalocyanine/TiO2 and porphyrin/TiO2 catalysed processes, Molecules 20 (1) (2015) 396–415.
[48] K. Lorber, P. Djinovic, Accelerating photo-thermal CO2 reduction to CO, CH4 or methanol over metal/oxide semiconductor catalysts, iScience 25 (4) (2022).
[49] J.X. Zhu, et al., Recent advances in Cu-based cocatalysts toward solar-to-hydrogen evolution: categories and roles, Sol. RRL 3 (10) (2019).
[50] S. Cao, et al., Visible light driven photo-reduction of Cu2+ to Cu2O to Cu in water for photocatalytic hydrogen production, RSC Adv. 10 (10) (2020) 5930–5937.
[51] C.V. Montoya-Bautista, et al., Characterization and evaluation of copper slag as a bifunctional photocatalyst for alcohols degradation and hydrogen production, Top. Catal. 64 (1) (2021) 131–141.
[52] A.-A. Morales-Pérez, et al., Simultaneous hydrogen production and acetic acid degradation by heterogeneous photocatalysis using a metallurgical waste as catalyst, Top. Catal. 64 (1) (2021) 17–25.